Prepared for submission to JHEP
March 2, 2022

FR-PHENO-2019-001
Cavendish-HEP-19/05
TIF-UNIMI-2019-1
VBSCAN-PUB-02-19

QCD and electroweak corrections to WZ scattering at the LHC

Ansgar Denner[1], **Stefan Dittmaier**[2], **Philipp Maierhöfer**[2], **Mathieu Pellen**[3], **Christopher Schwan**[2,4]

[1] *Universität Würzburg, Institut für Theoretische Physik und Astrophysik, Emil-Hilb-Weg 22, 97074 Würzburg, Germany*

[2] *Universität Freiburg, Physikalisches Insitut, Hermann-Herder-Straße 3, 79104 Freiburg, Germany*

[3] *University of Cambridge, Cavendish Laboratory, Cambridge CB3 0HE, United Kingdom*

[4] *Tif Lab, Dipartimento di Fisica, Università di Milano and INFN, Sezione di Milano, Via Celoria 16, 20133 Milano, Italy*

E-mail: ansgar.denner@physik.uni-wuerzburg.de, stefan.dittmaier@physik.uni-freiburg.de, philipp.maierhoefer@physik.uni-freiburg.de, mpellen@hep.phy.cam.ac.uk, christopher.schwan@mi.infn.it

Abstract: We present the first computation of the full next-to-leading-order QCD and electroweak corrections to the WZ scattering process at the LHC. All off-shell, gauge-boson-decay, and interference effects are taken into account for the process $pp \to \mu^+\mu^- e^+\nu_e jj + X$ at the orders $\mathcal{O}(\alpha_s\alpha^6)$ and $\mathcal{O}(\alpha^7)$. The electroweak corrections feature the typical Sudakov behaviour towards high energy and amount to -16% relative to the electroweak contribution to the integrated cross section. Moreover, the corrections induce significant shape distortions in differential distributions. The next-to-leading-order analysis of the quark- and gluon-induced channels is supplemented by a leading-order study of all possible contributions to the full $4\ell + 2$jets production cross section in a realistic fiducial phase-space volume.

Contents

1 Introduction

The accumulation of experimental data during Run II of the Large Hadron Collider (LHC) allows to measure some rare Standard Model (SM) processes for the first time. Vector-boson scattering (VBS) processes constitute a prime example of processes that have not been measured before Run II. While the scattering of like-sign W-boson pairs, the golden VBS channel, has been measured first [1–5], the WZ channel comes in second [6, 7]. It features a lower cross section than $W^{\pm}W^{\pm}$ scattering, but has only one neutrino in the final state, allowing thus for better reconstruction and a better study of its properties.

As experimental errors (both statistical and systematic) will shrink in the next few years, precise theoretical predictions should be carefully prepared. In particular, higher-order corrections of both QCD and electroweak (EW) type should be incorporated. The inclusion of next-to-leading-order (NLO) QCD corrections has become standard for LHC analyses, but not yet the inclusion of EW corrections, which are known to increase at high energies owing to Sudakov logarithms. For the class of VBS processes, EW corrections are expected to be particularly large [8]. This expectation was confirmed in the first complete NLO QCD+EW calculation presented in Ref. [9] for like-sign WW scattering where it turned out that the genuine EW corrections of order $\mathcal{O}(\alpha^7)$ are even the largest NLO contribution.

In this article, we present results for the first calculation of the full NLO QCD+EW corrections to the WZ scattering process at the LHC with the final state $\mu^+\mu^-e^+\nu_e jj$. An analysis of the LO contributions to the WZjj production mode was presented in Ref. [10], where also different Monte Carlo programs were compared. In our NLO analysis, we include the whole set of contributing diagrams in the relevant orders, instead of only VBS configurations. The QCD and especially the EW corrections are rather involved, as the process features seven charged external particles. This is the first time that EW corrections are computed for a process involving so many charged particles. The leptonic final state with a single net charge gives rise to a larger number of partonic channels as compared to like-sign WW VBS, which complicates the calculation further. We also note that our calculation of QCD corrections is based on the full set of NLO diagrams including all interferences without approximation, *i.e.* we do not employ the so-called VBS approximation used in previous QCD calculations [11, 12], which neglects colour exchange between the two incoming protons. While for the current experimental precision such approximations are most likely sufficient, in the future they might actually be inadequate, because they can fail at the level of 10% in differential distributions, as shown in Ref. [13] for like-sign WW scattering.

In addition to the contributions to the NLO cross section of orders $\mathcal{O}(\alpha_s\alpha^6)$ and $\mathcal{O}(\alpha^7)$, we also provide predictions for all LO processes relevant for the $\mu^+\mu^-e^+\nu_e jj$ final state. These include the orders $\mathcal{O}(\alpha^6)$ (EW contribution), $\mathcal{O}(\alpha_s\alpha^5)$ (interference), and $\mathcal{O}(\alpha_s^2\alpha^4)$ (QCD contribution). Contributions including photons in the initial state or external bottom quarks are discussed separately.

All these results are presented in the form of cross sections and differential distributions for realistic experimental cuts. Specifically, the event selection chosen is the so-called *loose fiducial* region presented by the CMS collaboration in Ref. [7]. It has the advantage to be simple enough to be implemented easily in a Monte Carlo program. Such an experimental

effort is particularly welcome by theorists as it allows for a direct use of state-of-the-art theoretical predictions in experimental analyses.

Finally, we would like to mention that all results have been produced by two independent Monte Carlo programs, matrix elements providers, and loop libraries: One is the Monte Carlo program BONSAY with matrix elements from OpenLoops [14, 15] and loop integrals evaluated with the DD mode of the Collier [16, 17] library. The other Monte Carlo is MoCaNLO with matrix elements from Recola [18, 19] and loop integrals evaluated with the COLI mode of the Collier library. The two independent calculations ensure a exhaustive validation of all results presented in this paper.

This article is organised as follows: In Section 2, the various contributions to the NLO cross section of the considered process are described. In Section 3 the details on the implementations of the computation as well as the checks performed to validate the results are presented. Section 4 is devoted to the description and the analysis of the results. Finally, Section 5 contains a summary of the article as well as concluding remarks.

2 Definition of the process and survey of cross-section contributions

2.1 Leading-order contributions

As for all quark–quark-initiated processes characterised by four leptons and two jets in the final state, two types of amplitudes occur for the quark-induced processes $\mathrm{qq} \to \mu^+\mu^-\mathrm{e}^+\nu_\mathrm{e}\mathrm{qq}$, where q generically stands for a quark or antiquark: These are diagrams of order $\mathcal{O}(g^6)$ (some sample diagrams are shown in Figures 1a–1f) and diagrams of order $\mathcal{O}(g_\mathrm{s}^2 g^4)$ (an example is depicted in Figure 1g), with g_s and g generically denoting the strong and electroweak gauge couplings, respectively. Besides VBS the former diagrams involve also the production of three vector bosons as well as singly-resonant and non-resonant diagrams. Consequently, three different orders contribute to the LO cross section: $\mathcal{O}(\alpha^6)$ (EW contribution), $\mathcal{O}(\alpha_\mathrm{s}\alpha^5)$ (interference), and $\mathcal{O}(\alpha_\mathrm{s}^2\alpha^4)$ (QCD contribution).

At the order $\mathcal{O}(\alpha^6)$, where all couplings are of EW origin, there are in addition contributions from $\gamma\gamma \to \mu^+\mu^-\mathrm{e}^+\nu_\mathrm{e}\mathrm{qq}$ (Figure 1h provides an example). For the quark contributions, one can further distinguish the cases in which an external quark is a bottom quark or a light one. In our predictions, we show separately the $\mathcal{O}(\alpha^6)$ contributions with an external bottom quark, as the corresponding partonic channels can develop a top-quark resonance (see Figure 1f). The photon-induced contributions are also shown separately.

The order $\mathcal{O}(\alpha_\mathrm{s}\alpha^5)$ contributions are obtained by interfering amplitudes of $\mathcal{O}(g^6)$ and $\mathcal{O}(g_\mathrm{s}^2 g^4)$ in the channels $\mathrm{qq} \to \mu^+\mu^-\mathrm{e}^+\nu_\mathrm{e}\mathrm{qq}$. Further contributions in this order result from squares of amplitudes of order $\mathcal{O}(g_\mathrm{s} g^5)$ of the channels $\mathrm{g}\gamma \to \mu^+\mu^-\mathrm{e}^+\nu_\mathrm{e}\mathrm{qq}$ and $\mathrm{q}\gamma \to \mu^+\mu^-\mathrm{e}^+\nu_\mathrm{e}\mathrm{qg}$ (see Figures 1i and 1j for examples). Those contributions are shown together with the order $\mathcal{O}(\alpha^6)$ photon-induced contributions.

Finally, the $\mathcal{O}(\alpha_\mathrm{s}^2\alpha^4)$ contributions result from channels with either four external quarks or two external quarks and two gluons (see Figures 1k and 1l for examples). The contribution with two gluons in the initial state is particularly large due to the large gluonic parton-distribution function (PDF) at the LHC. The order $\mathcal{O}(\alpha_\mathrm{s}^2\alpha^4)$ contributions

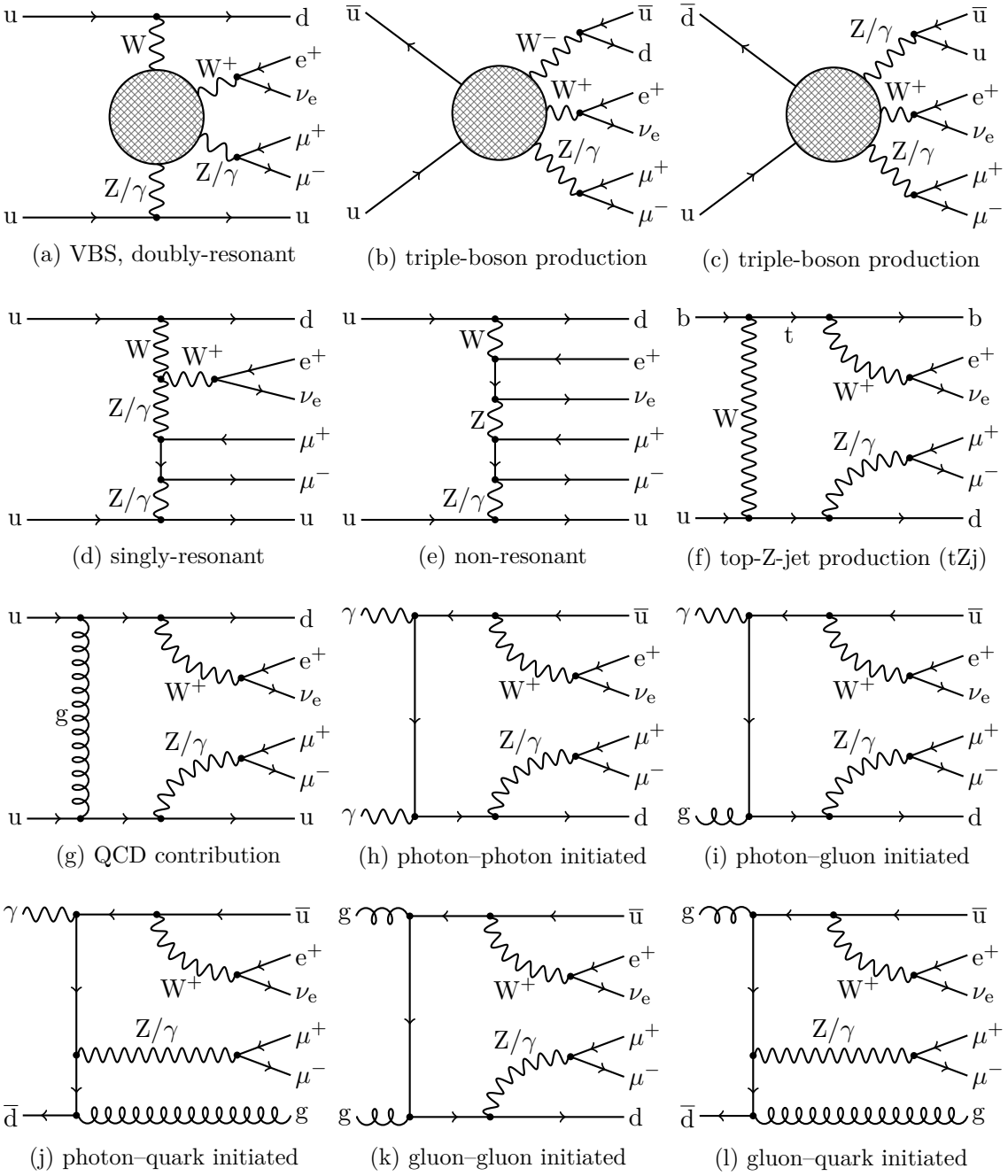

Figure 1: Examples of LO Feynman diagrams.

with external bottom quarks are shown separately, in combination with the order $\mathcal{O}(\alpha^6)$ bottom-quark contributions.

2.2 Virtual corrections

We compute the NLO corrections of orders $\mathcal{O}(\alpha^7)$ and $\mathcal{O}(\alpha_s\alpha^6)$ for the process

$$\mathrm{pp} \to \mu^+\mu^-\mathrm{e}^+\nu_\mathrm{e}\mathrm{jj} + X. \tag{2.1}$$

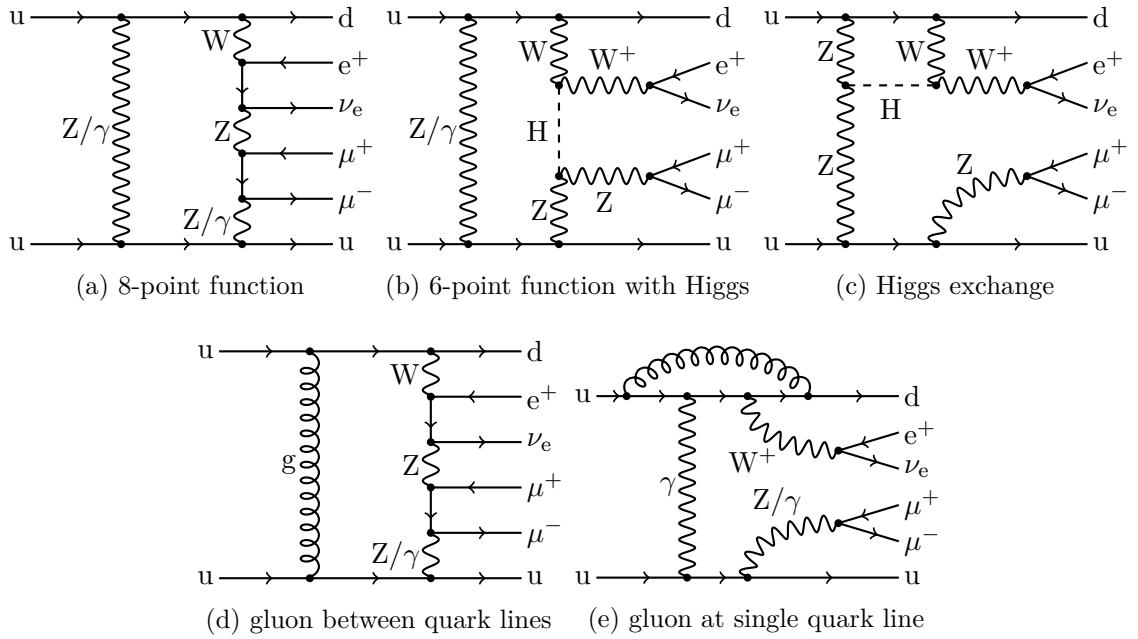

(a) 8-point function (b) 6-point function with Higgs (c) Higgs exchange

(d) gluon between quark lines (e) gluon at single quark line

Figure 2: Example loop diagrams.

Virtual corrections of order $\mathcal{O}(\alpha^7)$ result from interferences of the tree-level EW diagrams of order $\mathcal{O}(g^6)$ with purely EW loop diagrams of order $\mathcal{O}(g^8)$. Examples for the latter are depicted in Figures 2a–2c. The virtual corrections of order $\mathcal{O}(\alpha_s\alpha^6)$ receive contributions from several sources. EW loop diagrams for quark-induced processes of order $\mathcal{O}(g^8)$ (Figures 2a–2c) interfere with LO diagrams of order $\mathcal{O}(g_s^2 g^4)$ (Figure 1g). Due to the SU(3) colour structure, this only gives a non-vanishing contribution for partonic processes where all external quarks belong to the same generation. Loop diagrams of order $\mathcal{O}(g_s^2 g^6)$ (like in Figures 2d–2e) interfere with EW LO diagrams. Owing to the colour structure, in case of two different generations of quarks in the partonic process, only diagrams of the type Figure 2e with gluon exchange within one quark line contribute. In both types of NLO corrections, partonic channels with initial-state photons are not taken into account, since their contribution is already strongly suppressed at LO. Channels with external bottom quarks are excluded as well. Those could only significantly contribute via singly-resonant top quarks, which corresponds to a different experimental signature. In total, 40 partonic channels must be taken into account at each coupling order with up to $\sim$ 83,000 1-loop Feynman diagrams contributing per channel. Tensor integrals appear up to 8-point functions with tensor ranks of up to 4.

In the VBS approximation, as employed in previous QCD calculations, only QCD corrections of the type Figure 2e with gluon exchange within one quark line are taken into account. With $\sim$ 1000 Feynman diagrams per partonic channel and up to 5-point functions this approximation reduces the complexity drastically in comparison to the calculation presented in this article.

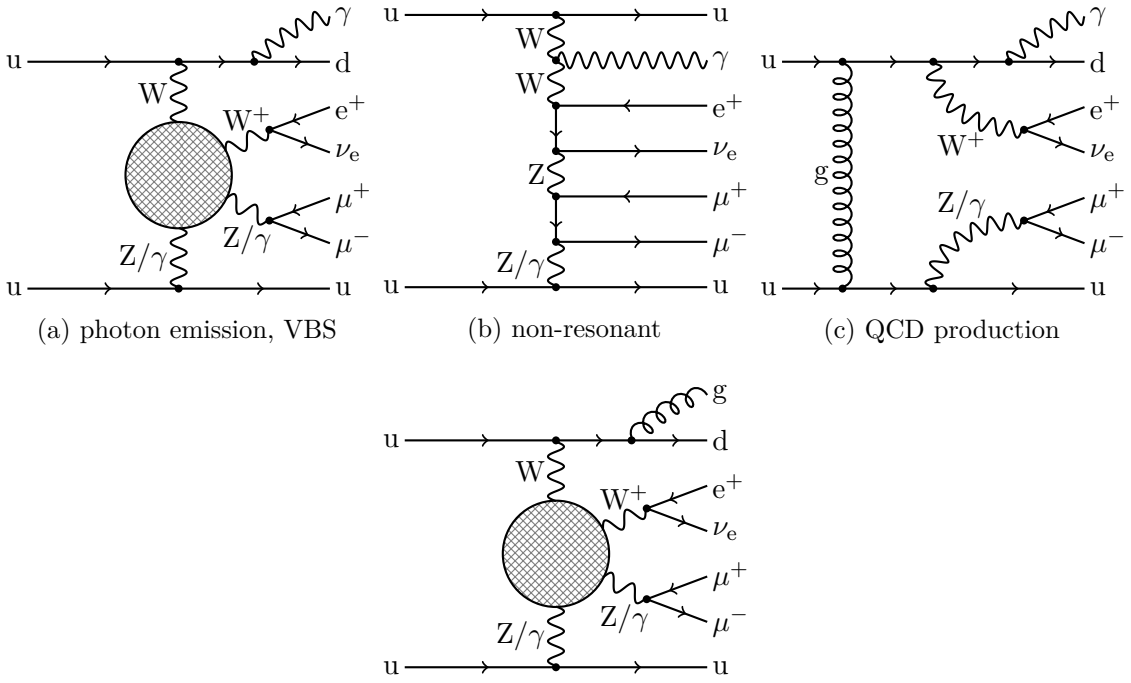

(a) photon emission, VBS (b) non-resonant (c) QCD production

(d) gluon emission, VBS

Figure 3: Sample diagrams for real corrections.

2.3 Real corrections

At the order $\mathcal{O}(\alpha^7)$, there are two types of real EW corrections: One is due to photon radiation, which results from radiating a photon from one of the charged particles of the LO processes of order $\mathcal{O}(\alpha^6)$. The other type comprises photon-induced channels, which we do not take into account at NLO, as already the corresponding LO contribution turned out to be very small.[1] Therefore, only real photon radiation from the $\mathrm{qq} \to \mu^+\mu^-\mathrm{e}^+\nu_\mathrm{e}\mathrm{qq}$ channels, *i.e.* the process $\mathrm{qq} \to \mu^+\mu^-\mathrm{e}^+\nu_\mathrm{e}\mathrm{qq}\gamma$, is considered. Some relevant Feynman diagrams are shown in Figures 3a and 3b. The related infrared (IR) divergences are subtracted using QED dipole subtraction [20, 21].

At the order $\mathcal{O}(\alpha_\mathrm{s}\alpha^6)$ a mixture of two types of real radiation contributes, because this NLO contribution comprises both QCD corrections to the order $\mathcal{O}(\alpha^6)$ and EW corrections to the order $\mathcal{O}(\alpha_\mathrm{s}\alpha^5)$. The EW corrections are obtained by attaching a photon to each LO diagram of order $\mathcal{O}(g_\mathrm{s}^2 g^4)$ in all possible ways (see Figure 3c) and interfering the resulting diagrams with all photon emission diagrams of $\mathcal{O}(g^7)$. The QCD corrections are obtained by attaching a gluon to each LO diagram of order $\mathcal{O}(g^6)$ in all possible ways (a sample diagram is given in Figure 3d) resulting in the process $\mathrm{qq} \to \mu^+\mu^-\mathrm{e}^+\nu_\mathrm{e}\mathrm{qqg}$, and squaring the corresponding amplitude. Of course, there are also real QCD corrections of the same order with the gluon crossed into the initial state, $\mathrm{gq/qg} \to \mu^+\mu^-\mathrm{e}^+\nu_\mathrm{e}\mathrm{qqq}$. The phase-space integration for the real corrections of $\mathcal{O}(\alpha_\mathrm{s}\alpha^6)$ leads to both QCD and EW IR divergences

[1] In the case of same-sign W scattering, photon-induced corrections of order $\mathrm{O}(\alpha^7)$ have been found to be below 2 % [9]. They are expected to be of similar size for WZ scattering.

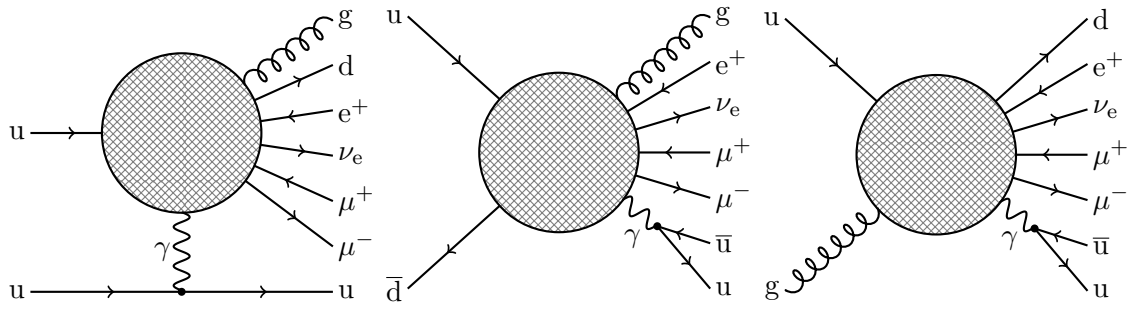

(a) initial-state coll. sing. (b) final-state coll. sing. (c) final-state coll. sing.

Figure 4: Photon singularities in the $\mathcal{O}(\alpha_s\alpha^6)$ real corrections.

in the limits of soft and/or collinear gluon or photon emission, or via forward branchings of QCD partons in the initial state. Figure 3a shows a $q \to q\gamma$ splitting of QED type, Figure 3d displays a typical $q \to qg$ splitting of QCD type.

For real radiation of order $\mathcal{O}(\alpha_s\alpha^6)$ further subtleties arise. Some diagrams with external real gluons involve singularities associated with soft/collinear photons. One example is given in Figure 4a which has an initial-state collinear singularity and requires both QED and QCD dipoles to subtract all IR divergences. Another subtle case arises from final states involving a $q\bar{q}$ pair. This pair can result from a QED splitting $\gamma^* \to q\bar{q}$ where the off-shell photon has a very low virtuality (see Figures 4b and 4c). In the singular limit where this virtuality goes to zero, a collinear singularity develops with a universal singular structure factorising from the hard matrix elements of the underlying process with a real photon instead of the $q\bar{q}$ pair. Note, however, that the physical final state is still a jet, or at least some hadronic activity, emerging from the photon initiating the splitting. Technically, the collinear singularity can, *e.g.*, be separated via dipole subtraction as described in Ref. [21], *i.e.* an auxiliary *subtraction function* is subtracted from the original integrand, rendering the resulting contribution integrable over the singular region. The formerly subtracted contribution is added back after integration over the singular region with the help of some regularisation, either by switching from four to D space–time dimensions or by employing small quark masses. Either way, the resulting singular contribution is not yet described in a physically meaningful way, since the splitting contains non-perturbative contributions. In the case of low-virtuality $\gamma^* \to q\bar{q}$ splittings, this contribution can be obtained from a dispersion integral for the R ratio of the cross sections for $e^+e^- \to \text{hadrons}/\mu^+\mu^-$, as will be further detailed in Ref. [22]. As described there, this contribution can be tied to the quantity $\Delta\alpha_{\text{had}}$, which is derived from experimental data. In our calculation we follow this approach, *i.e.* we separate the singularity via dipole subtraction [21] and add the non-perturbative fragmentation-like "photon-to-jets conversion part" from the collinear region based on $\Delta\alpha_{\text{had}}$. Conceptually, it is quite important to properly treat this non-perturbative contribution, but in the present case the overall contribution matters only at the level of 10^{-4} relative to the EW LO cross section.

Note that the previous discussion also applies in principle to the real corrections of order $\mathcal{O}(\alpha^7)$ with an additional photon. However, the extra collinear singularities coming

from the matrix elements similar to the ones in Fig. 4, but with external photons instead of gluons, are cut off due to our process definition. In particular, we treat a final-state photon in the real matrix elements always as a photon and never as a jet (or photon-jet). This choice implies that phase-space points with such collinear singularities have either zero or one jet. For final-state singularities, the two collinear quarks are clustered into a single jet while for an initial-state singularity, the collinear quark is along the beam pipe making it undetectable. Therefore our requirement of having at least two jets (see Section 4.1) cuts away such singularities, rendering the real corrections finite, so that no additional terms of type $\gamma \to q\bar{q}$ are required.

3 Details of the computation

3.1 Implementations

In order to ensure the correctness of the results, two independent Monte Carlo programs have been developed based on two entirely different sets of matrix elements constructed by independent matrix-element providers. One calculation is based on the combination BONSAY+OpenLoops, the other on MoCaNLO+Recola.

The program BONSAY is a general-purpose Monte Carlo integrator which can be used to calculate arbitrary NLO EW, QCD, and mixed corrections with matrix elements from an external provider. It has already been used before in Ref. [13] to calculate QCD corrections of like-sign WW scattering. It employs many different phase-space mappings that are combined via multi-channel techniques [23], similar to the Lusifer Monte Carlo program [24], but allows to run the integration in parallel on clusters using MPI [25].

MoCaNLO is also a generic Monte Carlo program, designed to compute arbitrary cross sections in the SM at NLO QCD and/or EW accuracy. The efficient integration is ensured by using phase-space mappings similar to the ones of Refs. [24, 26, 27]. It has already been used to compute NLO QCD and EW corrections for several high-multiplicity processes [28–31], including the like-sign W-boson VBS process [8, 9, 13]. Moreover, it has also been tested against other independent codes for the computation of EW corrections to di-boson production in Ref. [10].

In both Monte Carlo programs, IR divergences in the real radiation are handled with the dipole-subtraction method for QCD [32] and its extension to QED [20, 21]. Although the same algorithms are used, the two implementations are completely independent. The library LHAPDF [33] provides PDFs in both codes.

Both OpenLoops [14, 15] and Recola [18, 19] use the Collier library [16, 17] to obtain numerically stable results for the one-loop scalar [34–37] and tensor integrals [38–40]. In order to ensure independence, the two different modes of Collier have been used: the DD mode in BONSAY+OpenLoops and the COLI mode in MoCaNLO+Recola. The intermediate W/Z-boson resonances are treated in the complex-mass scheme [26, 41, 42] to ensure gauge independence of all LO and NLO amplitudes. In OpenLoops, we set the option `use_cms=2` to switch to the same conventions for the complex-mass scheme as used by Recola. This allows us to verify the agreement of the results of the two matrix-element providers for individual phase-space points.

The numerical results presented in this article are obtained from BONSAY,[2] which agrees with the other implementation within integration errors, which are typically of the size of a per mille with respect to the LO prediction.

3.2 Validation

The first and strongest validation is that the final results (at the level of cross sections and for each bin of the differential distributions) of the two calculations agree within statistical errors. This constitutes a very solid check as the two Monte Carlo programs as well as the matrix-element providers are different and independent. This ensures the correct implementation of the event selection, input parameters as well as the subtraction on the one hand. On the other hand, it also ensures the validity of the matrix elements used.

The α_{dipole} parameter [43] allows one to restrict the phase space to the singular regions, where $\alpha_{\text{dipole}} = 1$ corresponds to the full phase space (within the acceptance defined by selection cuts) without additional restrictions. Varying α_{dipole} allows then for a robust check of the subtraction procedure. Representative contributions have been checked between BONSAY+OpenLoops and MoCaNLO+Recola for $\alpha_{\text{dipole}} = 1$ for both orders $\mathcal{O}(\alpha_s\alpha^6)$ and $\mathcal{O}(\alpha^7)$. The final results have been obtained with $\alpha_{\text{dipole}} = 1$ for BONSAY+OpenLoops and $\alpha_{\text{dipole}} = 10^{-2}$ for MoCaNLO+Recola, showing agreement at the level of a per mille. This constitutes a strong check on the subtraction procedure used.

In addition, point-wise comparisons of (squared) matrix-element contributions have been carried out for the virtual corrections. At the order $\mathcal{O}(\alpha^7)$, which comprises the numerically most delicate loop amplitudes, for 1000 phase-space points chosen in the fiducial volume described above, more than 99% of the points show at least 6 digits of agreement. In total, the level of agreement spans from about 6 to 12 digits.

Finally, 1000 points have been generated to check the real QCD corrections. This ensures the correct implementation of the event selection for both the real radiation and the dipoles. In that way, the correct implementation of the dynamical scale is ensured as well.

4 Numerical results

4.1 Input parameters and event selection

The results presented are for the LHC operating at a centre-of-mass (CM) energy of 13 TeV. We use the NLO NNPDF 3.1 QED set [44, 45] with the photon PDF determined by the LUXqed method [46, 47] and $\alpha_s(M_Z) = 0.118$ (LHAPDF ID 324900), employing the fixed $N_F = 5$ flavour scheme throughout. We use the same PDFs for LO and NLO predictions. Both QCD and QED singularities from collinear initial-state splittings are factorised into redefined PDFs using the $\overline{\text{MS}}$ factorisation scheme.

[2] The only exception is the results of Table 4 for a centre-of-mass of 14 TeV which has been obtained from MoCaNLO.

The central renormalisation and factorisation scales, μ_{ren} and μ_{fact}, are set to the geometric average of the transverse momenta of the jets,

$$\mu_0 = \sqrt{p_{\text{T,j}_1}\, p_{\text{T,j}_2}}. \tag{4.1}$$

The choice of this scale is motivated by the results of Ref. [48] on like-sign WW scattering, where it was shown that this choice reduces the difference between LO and NLO QCD predictions at large transverse momenta significantly. In the following, we perform a 7-point scale variation of the renormalisation and factorisation scales, *i.e.* apart from the "diagonal" variations $\mu_{\text{ren}} = \mu_{\text{fact}} = \mu_0$, $\mu_0/2$, $2\mu_0$ we set each of the two scales to $\mu_0/2$, $2\mu_0$ while keeping the other scale fixed.

Regarding the electromagnetic coupling, the G_μ scheme (see, *e.g.* Refs. [49, 50]) is used, *i.e.* the coupling is obtained from the Fermi constant G_μ as

$$\alpha = \frac{\sqrt{2}}{\pi} G_\mu M_{\text{W}}^2 \left(1 - \frac{M_{\text{W}}^2}{M_{\text{Z}}^2}\right) \qquad \text{with} \qquad G_\mu = 1.16638 \times 10^{-5}\,\text{GeV}^{-2}. \tag{4.2}$$

The masses and widths of the massive particles read [51]

$$\begin{aligned} m_{\text{t}} &= 173.0\,\text{GeV}, & \Gamma_{\text{t}} &= 0\,\text{GeV}, \\ M_{\text{Z}}^{\text{OS}} &= 91.1876\,\text{GeV}, & \Gamma_{\text{Z}}^{\text{OS}} &= 2.4952\,\text{GeV}, \\ M_{\text{W}}^{\text{OS}} &= 80.379\,\text{GeV}, & \Gamma_{\text{W}}^{\text{OS}} &= 2.085\,\text{GeV}, \\ M_{\text{H}} &= 125.0\,\text{GeV}, & \Gamma_{\text{H}} &= 4.07 \times 10^{-3}\,\text{GeV}. \end{aligned} \tag{4.3}$$

The bottom quark is considered massless and is neglected in the initial state by default. The width of the top quark is set to zero as it is never resonant, except for the $\mathcal{O}(\alpha^6)$ contributions with external bottom quarks, which we consider separately; there we set the top-quark width to $\Gamma_{\text{t}}^{\text{LO}} = 1.449582\,\text{GeV}$ [52]. The Higgs-boson mass is taken according to the recommendation of the Higgs cross section working group [53] with its corresponding width. The pole masses and widths entering the calculation are determined from the measured on-shell (OS) values [54] for the W and Z bosons according to

$$M_V = \frac{M_V^{\text{OS}}}{\sqrt{1 + (\Gamma_V^{\text{OS}}/M_V^{\text{OS}})^2}}, \qquad \Gamma_V = \frac{\Gamma_V^{\text{OS}}}{\sqrt{1 + (\Gamma_V^{\text{OS}}/M_V^{\text{OS}})^2}}. \tag{4.4}$$

The set of acceptance cuts is taken from the recent CMS measurement, more precisely, the ones of the *loose fiducial* region defined in Ref. [7]. Experimentally, the final state of the process is required to have three charged leptons and at least two jets. QCD partons are clustered into jets using the anti-k_{T} algorithm [55] with jet-resolution parameter $R = 0.4$. Similarly, photons from real radiation are recombined with the final-state quarks into jets or with the charged leptons into dressed leptons, in both cases via the anti-k_{T} algorithm and a resolution parameter $R = 0.4$.

In MoCaNLO only partons with rapidity $|y| < 5$ are considered for recombination, while particles with larger $|y|$ are assumed to be lost in the beam pipe. In BONSAY all

partons are considered for recombination, regardless of their rapidities. This difference turns out to be numerically irrelevant in our set up.

The pseudo-rapidity η and the transverse momentum p_{T} of a particle are defined as

$$\eta = \frac{1}{2}\ln\left(\frac{|\mathbf{p}|+p_z}{|\mathbf{p}|-p_z}\right), \qquad p_{\mathrm{T}} = \sqrt{p_x^2+p_y^2}, \tag{4.5}$$

where $|\mathbf{p}|$ is the absolute value of the three-momentum $\mathbf{p}$ of the particle, p_z the component of its momentum along the beam axis, and p_x, p_y the components perpendicular to the beam axis.

The charged leptons ℓ are required to pass the acceptance cuts

$$p_{\mathrm{T},\ell} > 20\,\mathrm{GeV}, \qquad |\eta_\ell| < 2.5, \qquad M_{3\ell} > 100\,\mathrm{GeV}, \qquad M_{\ell\ell} > 4\,\mathrm{GeV}. \tag{4.6}$$

In addition, an invariant-mass cut on the decay products of the Z boson is applied:

$$|M_{\mu^+\mu^-} - M_{\mathrm{Z}}| < 15\,\mathrm{GeV}. \tag{4.7}$$

A recombined QCD parton system is called a jet if it obeys the jet-identification criteria

$$p_{\mathrm{T,j}} > 30\,\mathrm{GeV}, \qquad |\eta_{\mathrm{j}}| < 4.7, \qquad \Delta R_{\mathrm{j}\ell} > 0.4, \tag{4.8}$$

where the last condition requires a minimal distance between a jet and each of the charged leptons. The identified jets are then ordered according to the magnitude of their transverse momenta $p_{\mathrm{T,j},i}$, where $p_{\mathrm{T,j},1}$ denotes the largest $p_{\mathrm{T,j}}$ value in the event and $p_{\mathrm{T,j},2}$ the second largest. The distance ΔR_{ij} between two particles i and j in the pseudo-rapidity–azimuthal-angle plane reads

$$\Delta R_{ij} = \sqrt{(\Delta\phi_{ij})^2 + (\Delta\eta_{ij})^2}, \tag{4.9}$$

with $\Delta\phi_{ij} = \min(|\phi_i - \phi_j|, 2\pi - |\phi_i - \phi_j|)$ being the azimuthal-angle difference and $\Delta\eta_{ij} = \eta_i - \eta_j$ the rapidity difference. On the invariant-mass and rapidity separation of the leading and sub-leading jets, *i.e.* on the two jets with largest transverse momenta, the following VBS cuts are applied:

$$M_{\mathrm{jj}} > 500\,\mathrm{GeV}, \qquad |\Delta y_{\mathrm{jj}}| > 2.5. \tag{4.10}$$

4.2 Cross sections

We start our discussion of numerical results by reporting LO cross sections in the fiducial region. In Table 1 the cross sections at the orders $\mathcal{O}(\alpha^6)$, $\mathcal{O}(\alpha_{\mathrm{s}}\alpha^5)$, and $\mathcal{O}(\alpha_{\mathrm{s}}^2\alpha^4)$ are shown for the central scale. In contrast to the like-sign WW channel, where the EW contribution largely dominates over the QCD one, here the EW contribution is smaller than the QCD contribution by about a factor four. The LO interference contribution of $\mathcal{O}(\alpha_{\mathrm{s}}\alpha^5)$ only amounts to 0.5 % and is, thus, phenomenologically unimportant.

Taking into account scale variation as defined after (4.1), the LO cross section for the quark-induced EW contribution (often referred to as signal in experimental analysis) is:

$$\sigma_{\mathrm{LO}}^{\mathcal{O}(\alpha^6)} = 0.25511(1)^{+9.0\,\%}_{-7.8\,\%}\ \mathrm{fb}. \tag{4.11}$$

Order	$\mathcal{O}(\alpha^6)$	$\mathcal{O}(\alpha_s\alpha^5)$	$\mathcal{O}(\alpha_s^2\alpha^4)$	Sum
σ_{LO}[fb]	0.25511(1)	0.006824(1)	1.0973(1)	1.3592(1)
Δ[%]	18.8	0.5	80.7	100

Table 1: LO cross sections σ_{LO} (sum) and individual orders $\mathcal{O}(\alpha^6)$, $\mathcal{O}(\alpha_s\alpha^5)$, and $\mathcal{O}(\alpha_s^2\alpha^4)$ for $pp \to \mu^+\mu^-e^+\nu_e jj+X$ at the LHC with CM energy 13 TeV. Photon-induced contributions and contributions with external bottom quarks are not included. Each contribution is given in fb and as fraction Δ relative to the sum of the three contributions (in percent). The digits in parentheses indicate the integration errors.

Note that this order does not involve any strong coupling, which explains the relatively low scale dependence. We do not show the scale dependence of the LO contribution at the orders $\mathcal{O}(\alpha_s\alpha^5)$ and $\mathcal{O}(\alpha_s^2\alpha^4)$, since the corresponding NLO contributions balancing their scale dependence are not part of this calculation.

In addition to these quark-induced EW contributions, we have also computed all LO contributions featuring a photon in the initial state. This includes contributions with initial states $g\gamma$, $q\gamma$ as well as $\gamma\gamma$ at orders $\mathcal{O}(\alpha^6)$ or $\mathcal{O}(\alpha_s\alpha^5)$. As can be seen from Table 2, these contributions are phenomenologically negligible. In addition, the LO contributions at order $\mathcal{O}(\alpha^6)$ involving bottom quarks either in the initial state or in the final state are also reported. While the contributions with two bottom quarks in the initial state are negligible due to their PDF suppression, the contributions with one light quark and one bottom quark in the initial state are rather large. The latter are usually referred to as $tZ + jet$ contributions in experimental analyses (see Figure 1f). These contributions are enhanced due to resonant top-quark contributions. In the final state they have one b-jet and one light jet and can therefore be suppressed in experimental analyses using b-jet tagging techniques.[3] Note that these contributions also contain VBS contributions (for instance diagram Figure 1a with the lower up-quark line replaced by a bottom quark line), but are dominated by contributions of a resonant top quark.

NLO cross sections including orders $\mathcal{O}(\alpha_s\alpha^6)$ or/and $\mathcal{O}(\alpha^7)$ in addition to the LO $\mathcal{O}(\alpha^6)$ are reported in Table 3 for the central scale as well as with the two extrema resulting from the 7-point scale variation. If only the $\mathcal{O}(\alpha^7)$ corrections are included the scale uncertainty remains at the same level as in LO, while the inclusion of the $\mathcal{O}(\alpha_s\alpha^6)$ corrections reduces the scale uncertainty as expected. The NLO contribution of order $\mathcal{O}(\alpha_s\alpha^6)$ amounts to about $-1.8\,\%$ with respect to the LO of order $\mathcal{O}(\alpha^6)$. As explained previously, this correction is of mixed type, *i.e.* it features both QCD and EW corrections. Nonetheless it is often referred to as QCD correction to the EW signal, as the VBS approximation neglects the (comparably small) EW corrections of order $\mathcal{O}(\alpha_s\alpha^6)$.

[3] In the WZ analysis of Ref. [7], such $tZ + jet$ contributions are suppressed by a central b-jet veto for $|\eta| < 2.5$. The residual contribution is then estimated from Monte Carlo simulations and subtracted as background. Conversely, the $tZ + jet$ process has recently been observed in Ref. [56] where the WZ EW contribution is considered as background. We have verified by a LO calculation that 91% of the tZ+jet contribution has a leading b-jet contained within $|\eta_b| < 2.5$.

Contribution	γ-induced	bottom
$\Delta\sigma_{\text{LO}}$[fb]	0.0009884(2)	0.19451(2)
$\Delta\sigma_{\text{LO}}/\sigma_{\text{LO}}^{\mathcal{O}(\alpha^6)}$[%]	0.4	76.2

Table 2: LO cross-section contributions $\Delta\sigma_{\text{LO}}$ for $\text{pp} \to \mu^+\mu^-\text{e}^+\nu_\text{e}\text{jj} + X$ with initial-state photons or external bottom quarks. The photon-induced contributions involve one or two initial-state photons and contribute to the orders $\mathcal{O}(\alpha^6)$ and $\mathcal{O}(\alpha_\text{s}\alpha^5)$. The "bottom" contributions are of the order $\mathcal{O}(\alpha^6)$ and $\mathcal{O}(\alpha_\text{s}^2\alpha^4)$, and involve bottom quarks in the initial and/or final state. All contributions are given in fb as well as relative to the LO EW cross section of order $\mathcal{O}(\alpha^6)$ (in percent). The digits in parentheses indicate the integration errors.

Order	$\mathcal{O}(\alpha^6) + \mathcal{O}(\alpha^7)$	$\mathcal{O}(\alpha^6) + \mathcal{O}(\alpha_\text{s}\alpha^6)$	$\mathcal{O}(\alpha^6) + \mathcal{O}(\alpha^7) + \mathcal{O}(\alpha_\text{s}\alpha^6)$
σ_{NLO}[fb]	0.2142(2)	0.2506(1)	0.2097(3)
$\sigma_{\text{NLO}}^{\text{max}}$[fb]	0.2325(3) [+8.5%]	0.2532(1) [+1.0%]	0.2125(2) [+1.3%]
$\sigma_{\text{NLO}}^{\text{min}}$[fb]	0.1984(2) [−7.4%]	0.2481(1) [−1.0%]	0.2050(3) [−2.2%]
δ[%]	−16.0	−1.8	−17.8

Table 3: Cross sections for $\text{pp} \to \mu^+\mu^-\text{e}^+\nu_\text{e}\text{jj} + X$ at the LHC with CM energy 13 TeV at NLO EW $[\mathcal{O}(\alpha^6) + \mathcal{O}(\alpha^7)]$, NLO QCD $[\mathcal{O}(\alpha^6) + \mathcal{O}(\alpha_\text{s}\alpha^6)]$, and NLO QCD+EW $[\mathcal{O}(\alpha^6) + \mathcal{O}(\alpha^7) + \mathcal{O}(\alpha_\text{s}\alpha^6)]$. Each contribution is given in fb (with the extrema resulting from scale variations as absolute numbers and as deviation in percent) and as relative correction $\delta = \sigma_{\text{NLO}}/\sigma_{\text{LO}}^{\mathcal{O}(\alpha^6)} - 1$ to the LO EW cross section of order $\mathcal{O}(\alpha^6)$ in percent. The digits in parentheses indicate the integration errors.

On the other hand, the EW corrections of order $\mathcal{O}(\alpha^7)$ amount to −16 % and represent the dominant NLO contribution. This is in line with the findings of Ref. [8] for like-sign WW scattering and supports the expectation that large EW corrections are an intrinsic feature of VBS at the LHC. Following Ref. [57], one can derive a leading logarithmic approximation for the EW corrections to the process $\text{pp} \to \mu^+\mu^-\text{e}^+\nu_\text{e}\text{jj} + X$ based on the logarithmic corrections to the sub-process $\text{WZ} \to \text{WZ}$. Taking the mixing of photon and Z boson into account and using $\mathcal{M}^{\text{WZ}\to\text{W}\gamma} \approx -\frac{s_\text{w}}{c_\text{w}}\mathcal{M}^{\text{WZ}\to\text{WZ}}$, one arrives at the approximation already given in Ref. [8] for $\text{WW} \to \text{WW}$. This approximation holds in fact for all scattering processes of EW bosons owing to the fact that these scattering processes result from the same $\text{SU}(2)_\text{w}$ coupling. The approximation reads

$$\text{d}\sigma_{\text{LL}} = \text{d}\sigma_{\text{LO}}\,(1 + \delta_{\text{EW,LL}})\,, \tag{4.12}$$

where

$$\delta_{\text{EW,LL}} = \frac{\alpha}{4\pi}\left\{-4C_W^{\text{EW}}\log^2\left(\frac{Q^2}{M_\text{W}^2}\right) + 2b_W^{\text{EW}}\log\left(\frac{Q^2}{M_\text{W}^2}\right)\right\} \tag{4.13}$$

Order	$\mathcal{O}(\alpha^6)$	$\mathcal{O}(\alpha^6)+\mathcal{O}(\alpha^7)$	$\mathcal{O}(\alpha^6)+\mathcal{O}(\alpha_s\alpha^6)$	NLO QCD+EW
σ[fb]	0.2988(6)	0.251(1)	0.294(1)	0.245(2)
$\sigma^{\max}$[fb]	0.3244(6)[+8.5%]	0.271(1)[+8.0%]	0.296(1)[+0.7%]	0.247(1)[+0.8%]
$\sigma^{\min}$[fb]	0.2767(6)[−7.4%]	0.233(1)[−7.2%]	0.291(1)[−1.0%]	0.243(2)[−0.8%]
δ[%]	—	−16.1	−1.8	−17.9

Table 4: Cross sections for $pp \to \mu^+\mu^-e^+\nu_e jj + X$ at the LHC with CM energy 14 TeV at LO [$\mathcal{O}(\alpha^6)$], NLO EW [$\mathcal{O}(\alpha^6)+\mathcal{O}(\alpha^7)$], NLO QCD [$\mathcal{O}(\alpha^6)+\mathcal{O}(\alpha_s\alpha^6)$], and NLO QCD+EW [$\mathcal{O}(\alpha^6)+\mathcal{O}(\alpha^7)+\mathcal{O}(\alpha_s\alpha^6)$]. Each contribution is given in fb (with the extrema resulting from scale variations as absolute numbers and as deviation in percent) and as relative correction $\delta = \sigma_{\rm NLO}/\sigma_{\rm LO}^{\mathcal{O}(\alpha^6)} - 1$ to the LO EW cross section of order $\mathcal{O}(\alpha^6)$ in percent. The digits in parentheses indicate the integration errors.

with $C_W^{\rm EW} = 2/s_{\rm w}^2$ and $b_W^{\rm EW} = 19/(6s_{\rm w}^2)$. The symbols $c_{\rm w}$ and $s_{\rm w}$ represent the cosine and sine of the weak mixing angle, respectively. The scale Q is a representative scale of the WZ → WZ scattering process; the four-lepton invariant mass $M_{4\ell}$ turns out to be particularly appropriate. Setting Q to the average LO value $\langle M_{4\ell}\rangle \simeq 413\,\text{GeV}$ and applying (4.13) to the integrated cross section, leads to a leading logarithmic correction of $\delta_{\rm EW,LL} = -17.5\%$, which is good given the approximation used. Applying $Q = M_{4\ell}$ event by event in the calculation results in $\delta_{\rm EW,LL} = -16.4\%$, which agrees even better with the result of the full calculation. As already noted in Ref. [8], the rather large average scale $\langle M_{4\ell}\rangle$ for VBS processes is not due to the peculiar VBS event selection but to an enhancement of the partonic qq' cross section containing the $VV' \to VV'$ subprocess resulting from a massive t-channel exchange [58]. It was verified for the related W^+W^+ scattering process that relaxing the cuts leaves the EW corrections at the same level.

Finally, the fiducial cross section with both NLO QCD and EW corrections added is

$$\sigma_{\rm NLO}^{\rm QCD+EW} = 0.2097(3)^{+1.3\,\%}_{-2.2\,\%}\ \text{fb}, \tag{4.14}$$

showing a significant reduction of scale uncertainty. This is mainly due to the $\mathcal{O}(\alpha_s)$ PDF redefinition included in the $\mathcal{O}(\alpha_s\alpha^6)$ NLO correction that cancels the factorisation scale dependence of the LO $\mathcal{O}(\alpha^6)$ contribution. As shown in Table 3, the full NLO correction is about −17.8 % with respect to the LO of order $\mathcal{O}(\alpha^6)$.

Finally, for completeness, we also provide cross sections at NLO for the LHC running at a centre-of-mass energy of 14 TeV in Table 4. While the LO cross section increases by 17.2% with respect to 13 TeV, the relative NLO corrections are rather stable. These numbers can be important for future operation of the LHC at high luminosity [59] and serve as benchmarks.

4.3 Differential distributions

In this section, LO predictions and NLO corrections for several differential distributions are discussed. We start with a few LO predictions in Figure 5. The upper panels show the

absolute predictions of order $\mathcal{O}(\alpha^6)$ (EW), $\mathcal{O}(\alpha_s\alpha^5)$ (interference), and $\mathcal{O}(\alpha_s^2\alpha^4)$ (QCD). In the lower panels, the relative contributions are displayed with respect to the sum of the three contributions. Note that the contributions featuring external bottom quarks or initial-state photons are not included here. The first two distributions are the invariant mass and pseudo-rapidity difference of the two tagging jets in Figures 5a and 5b. These observables are often used to separate EW and QCD contributions in experimental analysis. This is perfectly justified by the fact that at higher invariant mass or larger pseudo-rapidity, the EW contribution is becoming dominant. The effect of the event selection for $|\Delta\eta_{j_1j_2}| > 2.5$ and $|M_{j_1j_2}| > 500\,\text{GeV}$ is clearly visible. In Figure 5c, the transverse momentum of the second hardest jet is shown. Around 500 GeV, both the EW and QCD contributions become of the same size, as the QCD contribution is falling much more steeply than the EW contribution. Interestingly, this behaviour is not visible in other transverse-momentum and invariant-mass distributions, like the transverse-momentum distribution of the leading jet, where the QCD contributions are always larger than the EW contributions. The comparably steep fall of the distribution in the transverse momentum of the subleading jet is due to the fact that QCD contributions are dominated by contributions with at least one jet with small transverse momentum. Finally, Figure 5d displays the distribution in the rapidity–azimuthal-angle distance between the leading jets which also shows a good discriminating power, as already noticed in Ref. [10]. Note that in all distributions, the interference contribution is very much suppressed reflecting its overall small cross section.

The following figures show our results on NLO differential distributions. In the upper panels, the LO contribution of order $\mathcal{O}(\alpha^6)$ is shown along with the NLO predictions including orders $\mathcal{O}(\alpha^7)$ or/and $\mathcal{O}(\alpha_s\alpha^6)$. For simplicity, these are often denoted by EW and QCD corrections, respectively, in the following. We stress again that while the order $\mathcal{O}(\alpha^7)$ comprises genuine EW corrections, the order $\mathcal{O}(\alpha_s\alpha^6)$ contains both QCD and EW corrections. We adopt this assignment in order to facilitate the reading. For the QCD corrections, the lower panels show the relative contributions

$$\delta = \frac{\mathrm{d}\sigma(\mu)}{\mathrm{d}\sigma_{\text{LO}}^{\mathcal{O}(\alpha^6)}(\mu_0)} - 1, \tag{4.15}$$

where the bands in the plots reflect the variation of the numerator with the (renormalisation and/or factorisation) scale μ while keeping the scales in the denominator fixed to μ_0. For the EW corrections, only the value for the central scale is shown in the lower panels, because the scale dependence of the corresponding relative NLO contribution is negligible against the one of the other contributions. The larger scale variation of NLO QCD+EW with respect to NLO QCD in the plots results from the inclusion of the large EW NLO correction in the numerator of (4.15), where the μ-insensitive relative EW correction multiplies the scale-dependent LO cross section.

In Figure 6, several distributions in transverse momenta are presented. We start with those for the hardest and second hardest jet in Figures 6a and 6b, respectively. For both distributions, the EW corrections become large in size and negative for large transverse momenta. The QCD corrections are positive for low transverse momentum of the leading jet, but steadily decrease towards high transverse momentum, becoming negative above

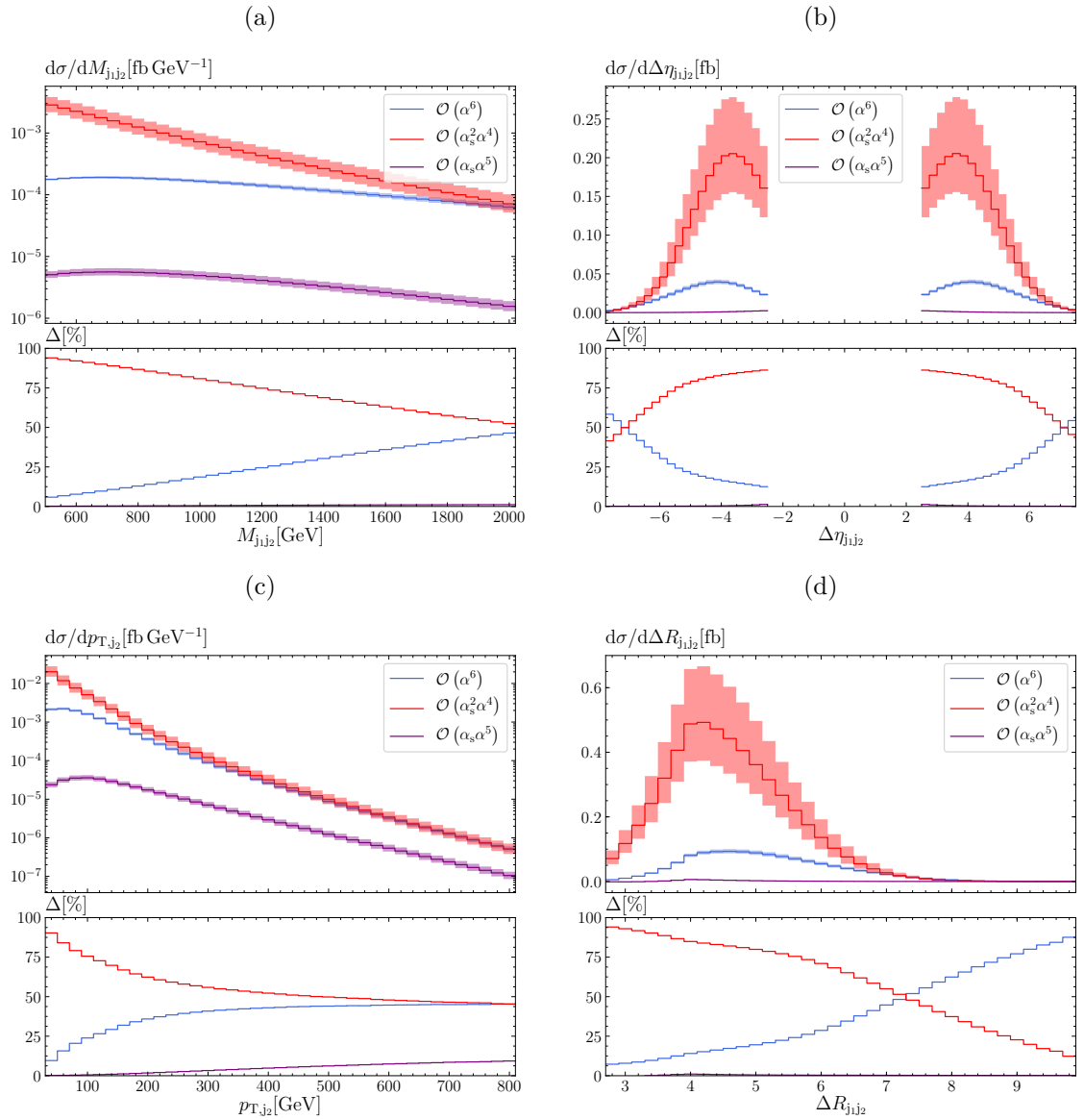

Figure 5: LO differential distributions for $pp \to \mu^+\mu^-e^+\nu_e jj + X$ at the LHC with CM energy 13 TeV: (a) invariant mass of the two jets (top left), (b) difference of pseudo-rapidity of the two jets (top right), (c) transverse momentum of the second hardest jet (bottom left), and (d) rapidity–azimuthal-angle distance between the two jets (bottom right). The upper panel shows the absolute contributions of order $\mathcal{O}(\alpha^6)$ (EW), $\mathcal{O}(\alpha_s\alpha^5)$ (interference), and $\mathcal{O}(\alpha_s^2\alpha^4)$ (QCD). The bands denote the envelope of the scale variation for each order. The lower panel shows the relative LO contributions Δ to their sum in percent.

150 GeV and stabilising in the range 200−300 GeV. This behaviour is typical of a process with hard jet emission in its signature and results from the reduction of the leading-jet transverse momentum by emission of real gluons and has also been observed in like-sign WW scattering [9]. For the transverse momentum of the second leading jet, the QCD corrections turn again positive towards high transverse momentum. The enhanced corrections for

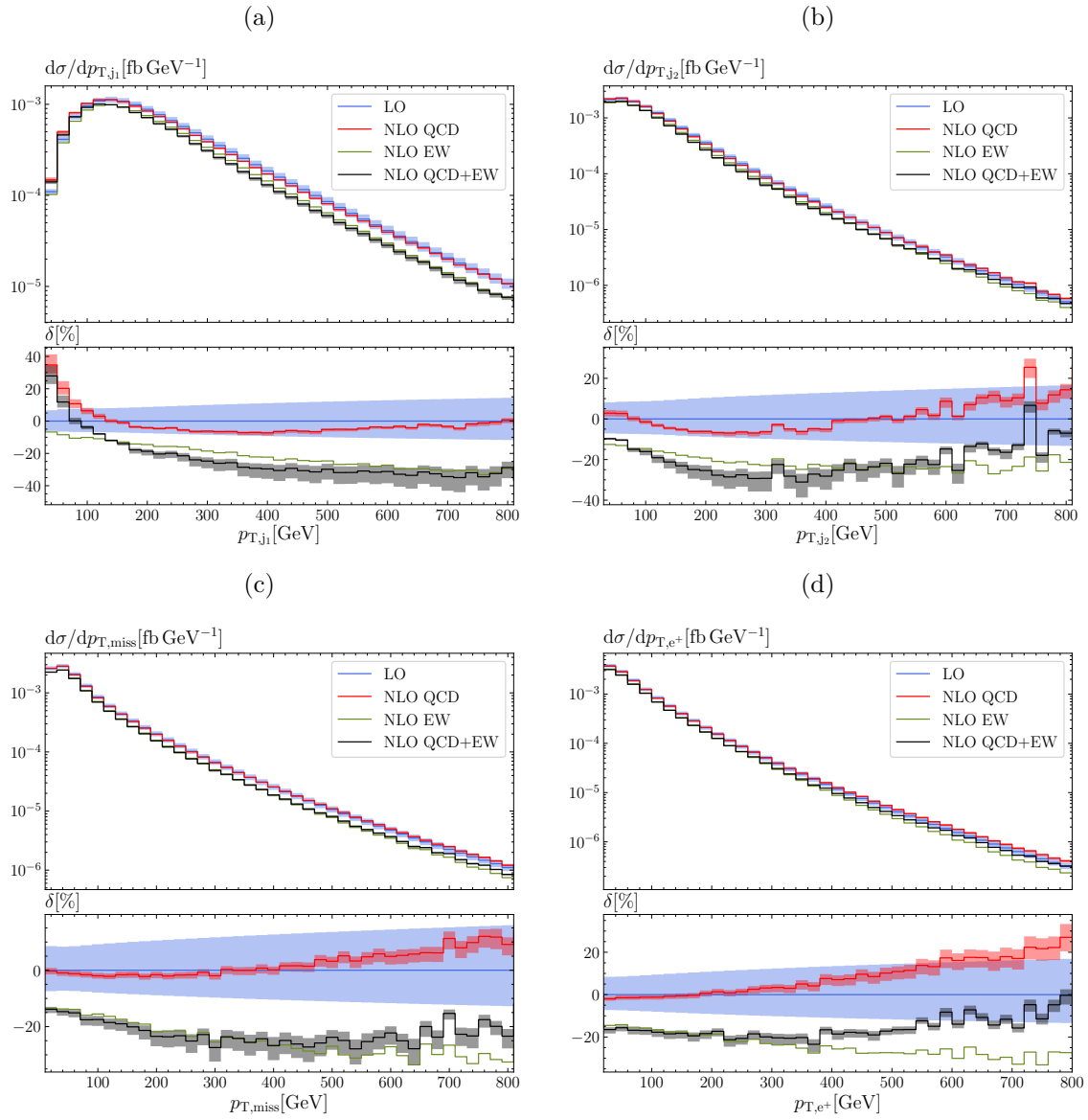

Figure 6: Differential distributions for $pp \to \mu^+\mu^- e^+\nu_e jj + X$ at the LHC with CM energy 13 TeV: (a) transverse momentum of the hardest jet (top left), (b) transverse momentum of the second hardest jet (top right), (c) missing transverse energy (bottom left), and (d) transverse momentum of the positron (bottom right). The upper panel shows the LO contributions of order $\mathcal{O}(\alpha^6)$, the two NLO predictions [including $\mathcal{O}(\alpha^7)$ (NLO EW) and $\mathcal{O}(\alpha_s\alpha^6)$ (NLO QCD)] as well as their sum. The lower panel shows the relative NLO corrections with respect to the LO in percent.

small transverse momentum of the leading jet are due to the phase-space suppression of the LO when all jet transverse momenta are required to be small. This causes corrections above 20% for small transverse momenta of the hardest jet, while the corrections almost vanish for small transverse momenta of the second hardest jet. For the distributions in the missing transverse momentum (Figure 6c), which is identified with the neutrino transverse

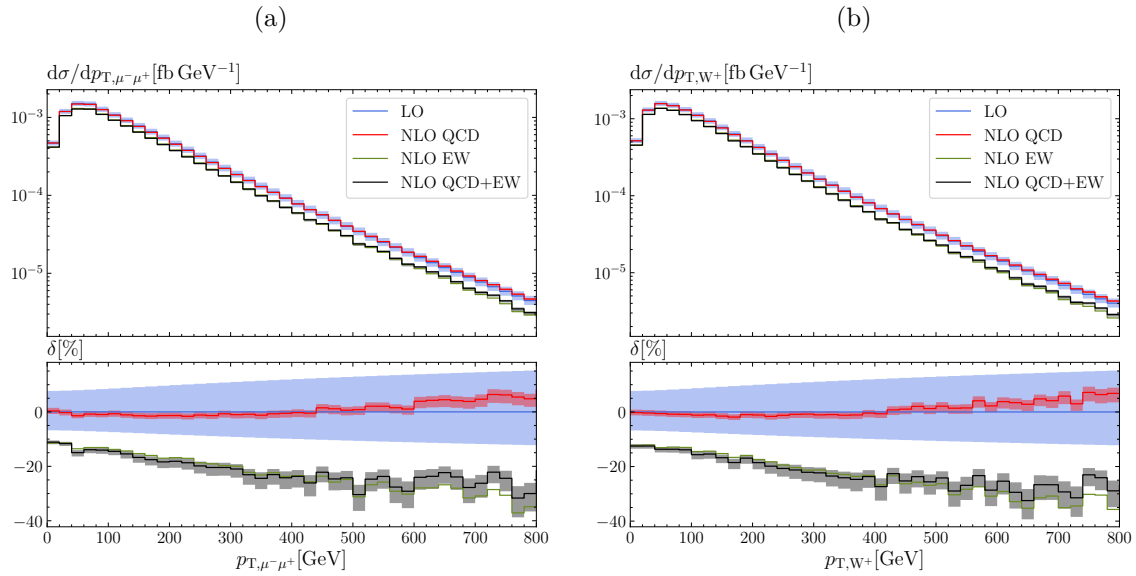

Figure 7: Differential distributions for $pp \to \mu^+\mu^-e^+\nu_e jj + X$ at the LHC with CM energy 13 TeV: (a) transverse momentum of the muon–anti-muon system (left) and(b) transverse momentum of the reconstructed W boson (right). The upper panel shows the LO contributions of order $\mathcal{O}(\alpha^6)$, the two NLO predictions [including $\mathcal{O}(\alpha^7)$ (NLO EW) and $\mathcal{O}(\alpha_s\alpha^6)$ (NLO QCD)] as well as their sum. The lower panel shows the relative NLO corrections with respect to the LO in percent.

momentum p_{T,ν_e}, and in the transverse momentum of the positron p_{T,e^+} (Figure 6d), the EW corrections increase negatively towards higher transverse momenta and exceed -25% at $p_T = 800\,\text{GeV}$. The QCD corrections are almost independent of $p_{T,\text{miss}}$ and p_{T,e^+} until about 400 GeV.

Since only the transverse momentum of one final-state particle becomes large in the distributions in Figure 6, the dominant kinematics is not necessarily in the Sudakov region, where all invariants are large. On the other hand, if the transverse momentum of one of the reconstructed gauge bosons gets large, the invariants of the dominating $VV' \to VV'$ scattering subprocess become large, and the Sudakov approximation applies to this subprocess. The distributions in the transverse momentum of the muon–anti-muon system shown in Figure 7a and in the reconstructed transverse momentum of the W boson in Figure 7b indeed display the typical Sudakov behaviour more clearly. The EW corrections rise monotonically to -35% at $p_T = 800\,\text{GeV}$. The QCD corrections, on the other hand, have a limited impact, reaching a maximum of only about 5% at 800 GeV.

In addition to the transverse momentum distributions of Fig. 6, we also show the reconstructed transverse momentum of the two gauge bosons in Fig. 7. In Fig. 7a, the transverse momentum of the muon–anti-muon system is shown while Fig. 7b displays the reconstructed transverse momentum of the W boson. The distributions display a similar behaviour for both the QCD and EW corrections. The QCD corrections have a limited impact, reaching a maximum of only about 5% at 800 GeV. On the other hand, the EW corrections show a monotonic behaviour, increasing negatively to reach -35% at 800 GeV.

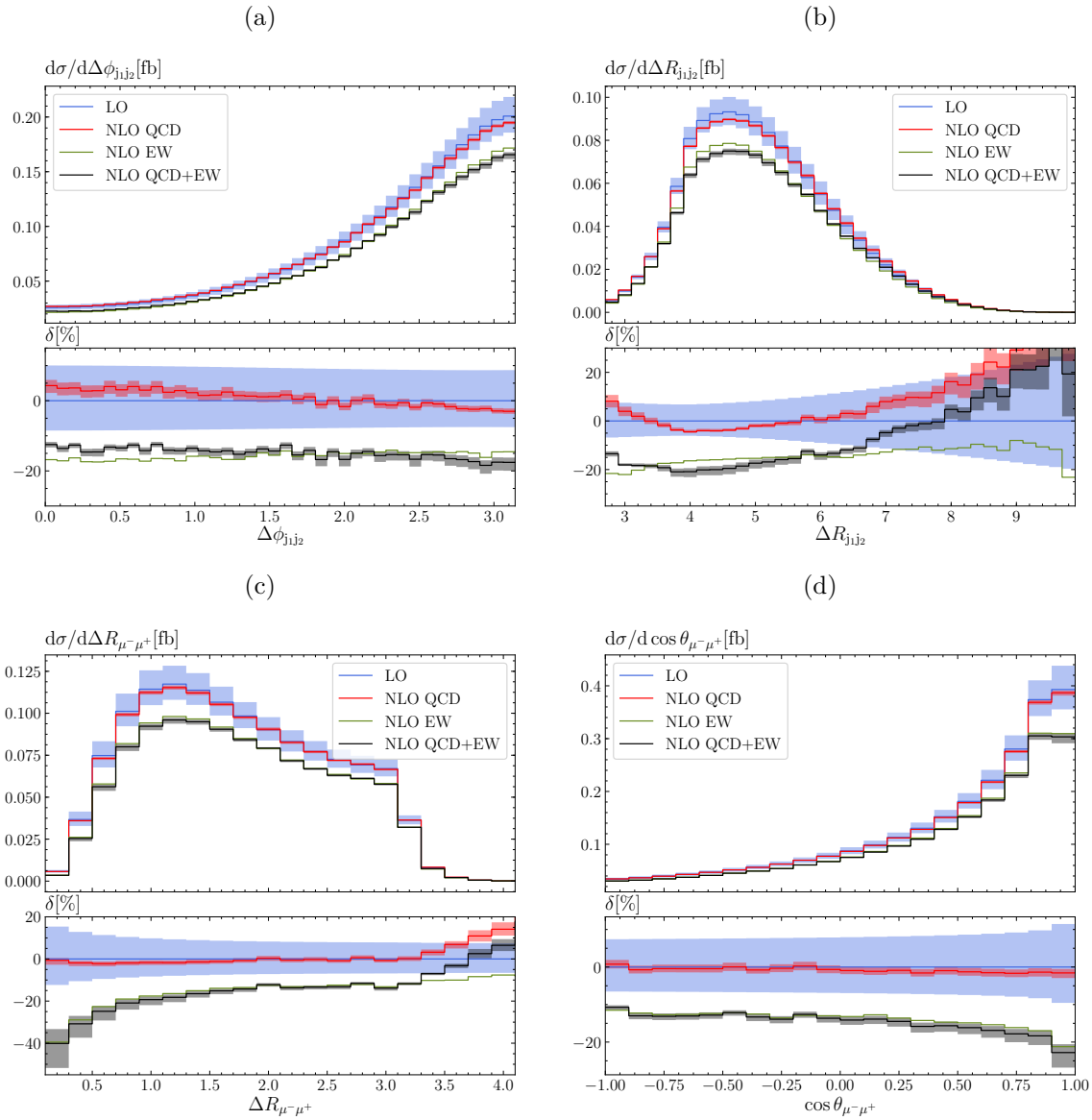

Figure 8: Differential distributions for $pp \to \mu^+\mu^-e^+\nu_e jj + X$ at the LHC with CM energy 13 TeV: (a) azimuthal angle between the two tagging jets (top left), (b) rapidity–azimuthal-angle distance between the two tagging jets (top right), (c) rapidity–azimuthal-angle distance between the muon and anti-muon (bottom left), and (d) cosine of the angle between the muon and anti-muon (bottom right). The upper panel shows the LO contributions of order $\mathcal{O}(\alpha^6)$, the two NLO predictions [including $\mathcal{O}(\alpha^7)$ (NLO EW) and $\mathcal{O}(\alpha_s\alpha^6)$ (NLO QCD)] as well as their sum. The lower panel shows the relative NLO corrections with respect to the LO in percent.

Such a behaviour is typical of EW Sudakov logarithms becoming large in the high-energy limit. Note that the other distributions shown later do not show such a pronounced Sudakov-logarithmic behaviour as they naturally inherit the intrinsic scale of the process.

Figure 8 displays some angular distributions. For the distribution in the azimuthal-

angle difference of the two tagging jets (Figure 8a) QCD and EW corrections follow a similar trend and inherit mostly the corrections to the total cross section. This does not hold for the other angular distributions, where the corrections show differences in shape. For the rapidity–azimuthal-angle distance between the two jets (Figure 8b), the QCD corrections reach a minimum around $\Delta R_{\mathrm{j_1 j_2}} = 4$, while the EW corrections tend to increase slightly towards increasing $\Delta R_{\mathrm{j_1 j_2}}$, resulting in an increase of the combined NLO prediction. The QCD corrections are generally flat and small for distributions in leptonic angular variables, resulting in combined predictions very close to the EW ones. The distribution in the rapidity–azimuthal-angle distance of the muon and anti-muon (Figure 8c) displays increasing EW corrections with increasing $\Delta R_{\mu^-\mu^+}$, varying from -45% at $\Delta R_{\mu^-\mu^+} \to 0$ to about -10% at $\Delta R_{\mu^-\mu^+} = 4$. The distribution in the cosine of the angle between the muon and anti-muon (Figure 8d) receives only a mild shape distortion towards $\cos\theta_{\mu^-\mu^+} \to 1$ from the EW corrections.

Figure 9 shows pseudo-rapidity distributions. The first two concern the hardest (Figure 9a) and second hardest jet (Figure 9b). Both QCD and EW corrections are rather similar in shape and differ mainly by some offset. For the hardest jet, the corrections peak in the peripheral region, while for the second hardest jet they increase in the central region as well. The distribution in the pseudo-rapidity of the anti-muon (Figure 9c) receives flat corrections over almost the whole range with only a slight increase in the peripheral region. Finally, both QCD and EW corrections increase with growing pseudo-rapidity difference of the two leading jets.

Finally, we show the distributions in the invariant mass of the two jets (Figure 10a) and in the transverse mass of the WZ system (Figure 10b). The invariant-mass distribution of the two jets displays a similar behaviour than the one in the transverse momentum of the jets: There is a steady increase in size of the negative EW corrections towards more and more negative values with increasing invariant masses due to EW high-energy logarithms. The QCD corrections are positive at 500 GeV and decrease slowly towards higher invariant masses. This is particularly interesting, as this observable is used to define fiducial regions in measurements. The transverse mass $M_{\mathrm{T,W^+Z}}$, of the WZ system is defined as

$$M^2_{\mathrm{T,W^+Z}} = \Big(\sum_\ell p_{\mathrm{T},\ell}\Big)^2 - \Big(\sum_\ell p_{x,\ell}\Big)^2 - \Big(\sum_\ell p_{y,\ell}\Big)^2, \tag{4.16}$$

where ℓ is running over the four leptons (including the neutrino). In the region below $M_{\mathrm{W}} + M_{\mathrm{Z}}$, which does not receive contributions from doubly-resonant WZ pairs, QCD and EW corrections are flat, while for large transverse masses the Sudakov logarithms dominate the EW corrections. The QCD corrections turn out to be small for the invariant-mass distributions.

5 Conclusion

The process $\mathrm{pp} \to \mu^+\mu^-\mathrm{e}^+\nu_\mathrm{e}\mathrm{jj} + X$ is of great interest at the LHC, because its EW contribution of order $\mathcal{O}(\alpha^6)$ to the cross section contains vector-boson scattering (VBS) as a subprocess. In this article we have reported on a calculation of NLO corrections

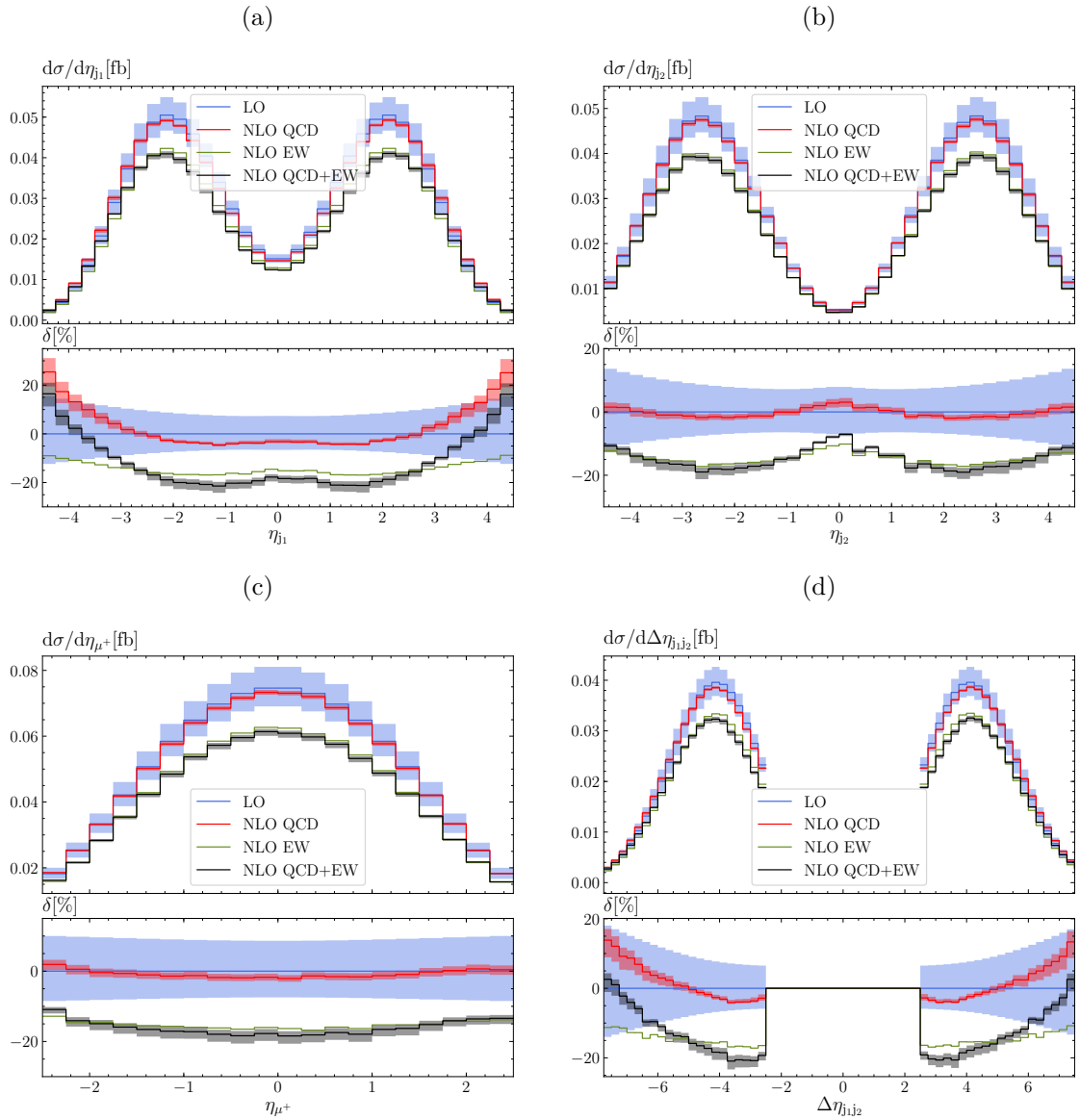

Figure 9: Differential distributions for $pp \to \mu^+\mu^- e^+\nu_e jj + X$ at the LHC with CM energy 13 TeV: (a) pseudo-rapidity of the hardest jet (top left), (b) pseudo-rapidity of the second hardest jet (top right), (c) pseudo-rapidity of the anti-muon (bottom left), and (d) difference of pseudo-rapidity of the two tagging jets (bottom right). The upper panel shows the LO contributions of order $\mathcal{O}(\alpha^6)$, the two NLO predictions [including $\mathcal{O}(\alpha^7)$ (NLO EW) and $\mathcal{O}(\alpha_s\alpha^6)$ (NLO QCD)] as well as their sum. The lower panel shows the relative NLO corrections with respect to the LO in percent.

of order $\mathcal{O}(\alpha_s\alpha^6)$ and $\mathcal{O}(\alpha^7)$ to the EW process. This is the first time that the EW corrections of $\mathcal{O}(\alpha^7)$ are computed for such a final state. While the QCD corrections of order $\mathcal{O}(\alpha_s\alpha^6)$ have already been computed in the VBS approximation [11], for the first time their full computation (including interference contributions of EW type) is performed. The combination of these two NLO contributions constitutes the complete NLO prediction

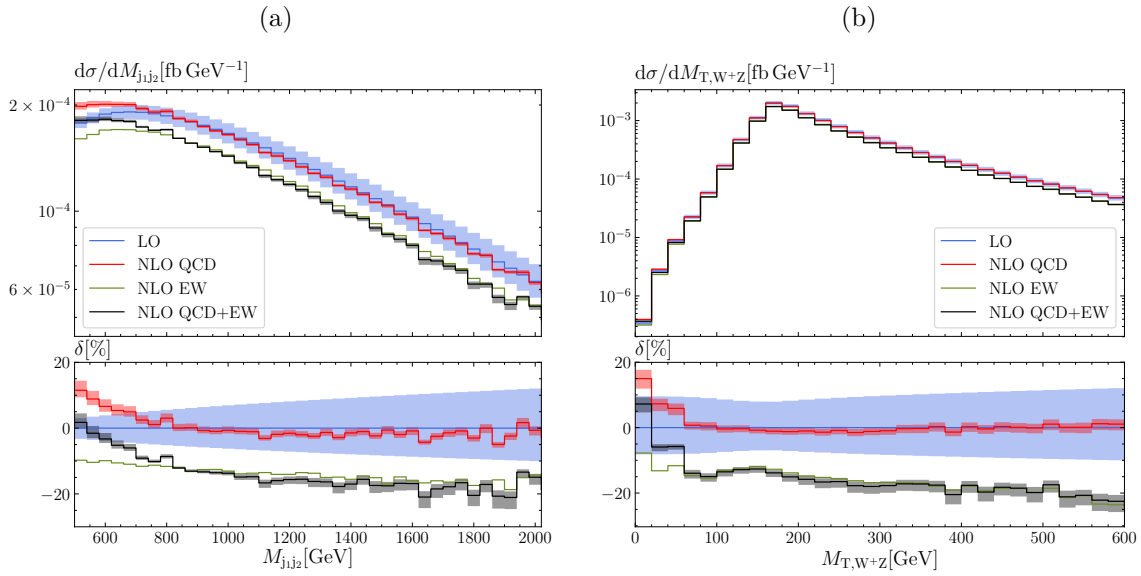

Figure 10: Differential distributions for $pp \to \mu^+\mu^-e^+\nu_e jj + X$ at the LHC with CM energy 13 TeV: (a) invariant mass of the two tagging jets (left), and (b) transverse mass of the four lepton system (right). The upper panel shows the LO contributions of order $\mathcal{O}(\alpha^6)$, the two NLO predictions [including $\mathcal{O}(\alpha^7)$ (NLO EW) and $\mathcal{O}(\alpha_s\alpha^6)$ (NLO QCD)] as well as their sum. The lower panel shows the relative NLO corrections with respect to the LO in percent.

for the EW component of the $pp \to \mu^+\mu^-e^+\nu_e jj + X$ process.

The EW corrections turn out to be relatively large, in accordance with similar observations made already for like-sign W scattering in Ref. [8]. This confirms the expectation that large EW corrections are indeed an intrinsic feature of VBS at the LHC. The corrections reach -16% in the chosen fiducial region and are driven by Sudakov logarithms that are large and negative and grow in size in the high-energy limit. The large EW corrections for the integrated fiducial cross section can be well reproduced by a simple logarithmic approximation. The corrections of order $\mathcal{O}(\alpha_s\alpha^6)$ (sometimes simply called QCD corrections) are small and negative. They amount to about -2% at the level of the integrated cross section and do not exceed 20% in differential distributions.

To complete the picture for the VBS process, we have also reported on several LO contributions, including some suppressed channels. The interference contribution of order $\mathcal{O}(\alpha_s\alpha^5)$ is below 1%, while the QCD contribution of order $\mathcal{O}(\alpha_s^2\alpha^4)$ is larger than the EW process by a factor 4. This shows how challenging the measurement of the EW process of order $\mathcal{O}(\alpha^6)$ is, highlighting therefore the need for precise predictions in this context. Moreover, we have computed all the LO contributions with a photon in the initial state. These turn out to be rather small and can safely be neglected in future analyses. Finally, we have computed the contributions involving bottom quarks (either both in the initial state or one in the final and one in the initial state) which turn out to be non-negligible. These are enhanced by contributions with a singly-resonant top quark, but can, in principle, be experimentally suppressed using b-tagging techniques.

In addition to the phenomenological relevance of the presented calculation, it is worth stressing that this also constitutes a non-trivial extension of previous computations. The complications arising here are manifold: (i) This is the first time that a process is computed at NLO EW accuracy with seven external charged particles. This increases the complexity of the real contribution as well as of the virtual corrections. (ii) The computation of the real contribution entails additional complications. QCD real radiation contains singular contributions arising from soft/collinear photons and gluons. This requires an advanced automation of computation of the real corrections. (iii) The number of partonic channels is very large. With respect to the like-sign W channel, the number of partonic channels increases by more than a factor three. This means that the computing time is considerably increased, and efficient book-keeping and parallelisation become decisive.

To come as close as possible to the situation realised in experimental analyses, our results are given in terms of integrated cross sections and differential distributions in the so-called *loose fiducial* region presented in Ref. [7] by the CMS collaboration. The event selections for this phase space are simplified with respect to the ones used for the actual measurement. Such efforts are particularly welcome to theorists as they allow a direct use of state-of-the-art theoretical progress in experimental analyses. Therefore the predictions provided in the present article should be particularly useful for the VBS program at the LHC.

Acknowledgements

AD and MP thank Jean-Nicolas Lang for supporting Recola. MP thanks Kenneth Long, Narei Lorenzo Martinez, Jakob Salfeld-Nebgen, and Marco Zaro for useful discussions. AD and MP acknowledge financial support by the German Federal Ministry for Education and Research (BMBF) under contracts no. 05H15WWCA1 and 05H18WWCA1 and the German Research Foundation (DFG) under reference number DE 623/6-1. SD and CS acknowledge support by the state of Baden-Württemberg through bwHPC and the DFG through grant no. INST 39/963-1 FUGG and grant DI 784/3. MP is supported by the European Research Council Consolidator Grant NNLOforLHC2. CS is supported by the European Research Council under the European Unions Horizon 2020 research and innovation Programme (grant agreement no. 740006). The authors would also like to acknowledge financial support from the COST Action CA16108.

References

[1] **ATLAS** Collaboration, G. Aad et al., *Evidence for Electroweak Production of $W^{\pm}W^{\pm}jj$ in pp Collisions at $\sqrt{s} = 8$ TeV with the ATLAS Detector*, *Phys. Rev. Lett.* **113** (2014) 141803, [arXiv:1405.6241].

[2] **CMS** Collaboration, V. Khachatryan et al., *Study of vector boson scattering and search for new physics in events with two same-sign leptons and two jets*, *Phys. Rev. Lett.* **114** (2015) 051801, [arXiv:1410.6315].

[3] **ATLAS** Collaboration, M. Aaboud et al., *Measurement of $W^{\pm}W^{\pm}$ vector-boson scattering and limits on anomalous quartic gauge couplings with the ATLAS detector*, *Phys. Rev.* **D96** (2017) 012007, [arXiv:1611.02428].

[4] **CMS** Collaboration, A. M. Sirunyan et al., *Observation of electroweak production of same-sign W boson pairs in the two jet and two same-sign lepton final state in proton-proton collisions at $\sqrt{s} = 13$ TeV*, *Phys. Rev. Lett.* **120** (2018) 081801, [arXiv:1709.05822].

[5] **ATLAS** Collaboration, "Observation of electroweak production of a same-sign W boson pair in association with two jets in pp collisions at $\sqrt{s}$ =13 TeV with the ATLAS detector." ATLAS-CONF-2018-030, 2018.

[6] **ATLAS** Collaboration, "Observation of electroweak $W^{\pm}Z$ boson pair production in association with two jets in pp collisions at $\sqrt{s} = 13$ TeV with the ATLAS Detector." ATLAS-CONF-2018-033, 2018.

[7] **CMS** Collaboration, A. M. Sirunyan et al., *Measurement of electroweak WZ boson production and search for new physics in WZ + two jets events in pp collisions at $\sqrt{s} = 13$ TeV*, arXiv:1901.04060.

[8] B. Biedermann, A. Denner, and M. Pellen, *Large electroweak corrections to vector-boson scattering at the Large Hadron Collider*, *Phys. Rev. Lett.* **118** (2017) 261801, [arXiv:1611.02951].

[9] B. Biedermann, A. Denner, and M. Pellen, *Complete NLO corrections to W^+W^+ scattering and its irreducible background at the LHC*, *JHEP* **10** (2017) 124, [arXiv:1708.00268].

[10] J. R. Andersen et al., *Les Houches 2017: Physics at TeV Colliders Standard Model Working Group Report*, in *10th Les Houches Workshop on Physics at TeV Colliders (PhysTeV 2017) Les Houches, France, June 5-23, 2017*, 2018. arXiv:1803.07977.

[11] G. Bozzi, B. Jäger, C. Oleari, and D. Zeppenfeld, *Next-to-leading order QCD corrections to W^+Z and W^-Z production via vector-boson fusion*, *Phys. Rev.* **D75** (2007) 073004, [hep-ph/0701105].

[12] B. Jäger, A. Karlberg, and J. Scheller, *Parton-shower effects in electroweak $WZjj$ production at the next-to-leading order of QCD*, *Eur. Phys. J.* **C79** (2019) 226, [arXiv:1812.05118].

[13] A. Ballestrero et al., *Precise predictions for same-sign W-boson scattering at the LHC*, *Eur. Phys. J.* **C78** (2018) 671, [arXiv:1803.07943].

[14] F. Cascioli, P. Maierhöfer, and S. Pozzorini, *Scattering Amplitudes with Open Loops*, *Phys. Rev. Lett.* **108** (2012) 111601, [arXiv:1111.5206].

[15] S. Kallweit, J. M. Lindert, P. Maierhöfer, S. Pozzorini, and M. Schönherr, *NLO electroweak automation and precise predictions for W+multijet production at the LHC*, *JHEP* **04** (2015) 012, [arXiv:1412.5157].

[16] A. Denner, S. Dittmaier, and L. Hofer, *COLLIER - A fortran-library for one-loop integrals*, *PoS* **LL2014** (2014) 071, [arXiv:1407.0087].

[17] A. Denner, S. Dittmaier, and L. Hofer, *COLLIER: a fortran-based Complex One-Loop LIbrary in Extended Regularizations*, *Comput. Phys. Commun.* **212** (2017) 220–238, [arXiv:1604.06792].

[18] S. Actis, A. Denner, L. Hofer, A. Scharf, and S. Uccirati, *Recursive generation of one-loop amplitudes in the Standard Model*, *JHEP* **04** (2013) 037, [arXiv:1211.6316].

[19] S. Actis, et al., *RECOLA: REcursive Computation of One-Loop Amplitudes*, *Comput. Phys. Commun.* **214** (2017) 140–173, [arXiv:1605.01090].

[20] S. Dittmaier, *A general approach to photon radiation off fermions*, *Nucl. Phys.* **B565** (2000) 69–122, [hep-ph/9904440].

[21] S. Dittmaier, A. Kabelschacht, and T. Kasprzik, *Polarized QED splittings of massive fermions and dipole subtraction for non-collinear-safe observables*, *Nucl. Phys.* **B800** (2008) 146–189, [arXiv:0802.1405].

[22] A. Denner, S. Dittmaier, M. Pellen, and C. Schwan, "Low-virtuality photon transitions $\gamma^* \to f\bar{f}$ and the photon-to-jet conversion function." In preparation.

[23] "A C++11 Template Library for Monte Carlo Integration." https://github.com/cschwan/hep-mc.

[24] S. Dittmaier and M. Roth, *LUSIFER: A LUcid approach to six FERmion production*, *Nucl. Phys.* **B642** (2002) 307–343, [hep-ph/0206070].

[25] "MPI Forum." https://www.mpi-forum.org/.

[26] A. Denner, S. Dittmaier, M. Roth, and D. Wackeroth, *Predictions for all processes $e^+e^- \to 4$ fermions $+\gamma$*, *Nucl. Phys.* **B560** (1999) 33–65, [hep-ph/9904472].

[27] F. A. Berends, R. Pittau, and R. Kleiss, *All electroweak four fermion processes in electron-positron collisions*, *Nucl. Phys.* **B424** (1994) 308–342, [hep-ph/9404313].

[28] A. Denner and R. Feger, *NLO QCD corrections to off-shell top-antitop production with leptonic decays in association with a Higgs boson at the LHC*, *JHEP* **11** (2015) 209, [arXiv:1506.07448].

[29] A. Denner and M. Pellen, *NLO electroweak corrections to off-shell top-antitop production with leptonic decays at the LHC*, *JHEP* **08** (2016) 155, [arXiv:1607.05571].

[30] A. Denner, J.-N. Lang, M. Pellen, and S. Uccirati, *Higgs production in association with off-shell top-antitop pairs at NLO EW and QCD at the LHC*, *JHEP* **02** (2017) 053, [arXiv:1612.07138].

[31] A. Denner and M. Pellen, *Off-shell production of top-antitop pairs in the lepton+jets channel at NLO QCD*, *JHEP* **02** (2018) 013, [arXiv:1711.10359].

[32] S. Catani and M. H. Seymour, *A general algorithm for calculating jet cross-sections in NLO QCD*, *Nucl. Phys.* **B485** (1997) 291–419, [hep-ph/9605323]. [Erratum: Nucl. Phys. **B510** (1998) 503].

[33] A. Buckley, et al., *LHAPDF6: parton density access in the LHC precision era*, *Eur. Phys. J.* **C75** (2015) 132, [arXiv:1412.7420].

[34] G. 't Hooft and M. J. G. Veltman, *Scalar one loop integrals*, *Nucl. Phys.* **B153** (1979) 365–401.

[35] W. Beenakker and A. Denner, *Infrared divergent scalar box integrals with applications in the electroweak Standard Model*, *Nucl. Phys.* **B338** (1990) 349–370.

[36] S. Dittmaier, *Separation of soft and collinear singularities from one-loop N point integrals*, *Nucl. Phys.* **B675** (2003) 447–466, [hep-ph/0308246].

[37] A. Denner and S. Dittmaier, *Scalar one-loop 4-point integrals*, *Nucl. Phys.* **B844** (2011) 199–242, [arXiv:1005.2076].

[38] G. Passarino and M. J. G. Veltman, *One-loop corrections for e^+e^- annihilation into $\mu^+\mu^-$ in the Weinberg Model*, *Nucl. Phys.* **B160** (1979) 151.

[39] A. Denner and S. Dittmaier, *Reduction of one-loop tensor 5-point integrals*, *Nucl. Phys.* **B658** (2003) 175–202, [hep-ph/0212259].

[40] A. Denner and S. Dittmaier, *Reduction schemes for one-loop tensor integrals*, *Nucl. Phys.* **B734** (2006) 62–115, [hep-ph/0509141].

[41] A. Denner, S. Dittmaier, M. Roth, and L. H. Wieders, *Electroweak corrections to charged-current $e^+e^- \to 4$ fermion processes: Technical details and further results*, *Nucl. Phys.* **B724** (2005) 247–294, [hep-ph/0505042]. [Erratum: Nucl. Phys. **B854** (2012) 504].

[42] A. Denner and S. Dittmaier, *The complex-mass scheme for perturbative calculations with unstable particles*, *Nucl. Phys. Proc. Suppl.* **160** (2006) 22–26, [hep-ph/0605312].

[43] Z. Nagy and Z. Trócsányi, *Next-to-leading order calculation of four-jet observables in electron-positron annihilation*, *Phys. Rev.* **D59** (1999) 014020, [hep-ph/9806317]. [Erratum: Phys. Rev. **D62** (2000) 099902].

[44] **NNPDF** Collaboration, R. D. Ball et al., *Parton distributions for the LHC Run II*, *JHEP* **04** (2015) 040, [arXiv:1410.8849].

[45] **NNPDF** Collaboration, V. Bertone, S. Carrazza, N. P. Hartland, and J. Rojo, *Illuminating the photon content of the proton within a global PDF analysis*, *SciPost Phys.* **5** (2018) 008, [arXiv:1712.07053].

[46] A. Manohar, P. Nason, G. P. Salam, and G. Zanderighi, *How bright is the proton? A precise determination of the photon parton distribution function*, *Phys. Rev. Lett.* **117** (2016) 242002, [arXiv:1607.04266].

[47] A. V. Manohar, P. Nason, G. P. Salam, and G. Zanderighi, *The Photon Content of the Proton*, *JHEP* **12** (2017) 046, [arXiv:1708.01256].

[48] A. Denner, L. Hošeková, and S. Kallweit, *NLO QCD corrections to W^+W^+jj production in vector-boson fusion at the LHC*, *Phys. Rev.* **D86** (2012) 114014, [arXiv:1209.2389].

[49] A. Denner, S. Dittmaier, M. Roth, and D. Wackeroth, *Electroweak radiative corrections to $e^+e^- \to WW \to 4$ fermions in double pole approximation: The RACOONWW approach*, *Nucl. Phys.* **B587** (2000) 67–117, [hep-ph/0006307].

[50] S. Dittmaier and M. Krämer, *Electroweak radiative corrections to W-boson production at hadron colliders*, *Phys. Rev.* **D65** (2002) 073007, [hep-ph/0109062].

[51] **ParticleDataGroup** Collaboration, M. Tanabashi et al., *Review of Particle Physics*, *Phys. Rev.* **D98** (2018) 030001.

[52] L. Basso, S. Dittmaier, A. Huss, and L. Oggero, *Techniques for the treatment of IR divergences in decay processes at NLO and application to the top-quark decay*, *Eur. Phys. J.* **C76** (2016) 56, [arXiv:1507.04676].

[53] **LHC Higgs Cross Section Working Group** Collaboration, J. R. Andersen et al., "Handbook of LHC Higgs Cross Sections: 3. Higgs Properties." CERN-2013-004, FERMILAB-CONF-13-667-T, 2013.

[54] D. Yu. Bardin, A. Leike, T. Riemann, and M. Sachwitz, *Energy-dependent width effects in e^+e^--annihilation near the Z-boson pole*, *Phys. Lett.* **B206** (1988) 539–542.

[55] M. Cacciari, G. P. Salam, and G. Soyez, *The anti-k_t jet clustering algorithm*, *JHEP* **04** (2008) 063, [arXiv:0802.1189].

[56] **CMS** Collaboration, A. M. Sirunyan et al., *Observation of single top quark production in association with a Z boson in proton-proton collisions at $\sqrt{s} = 13$ TeV*, *Phys. Rev. Lett.* **122** (2019) 132003, [arXiv:1812.05900].

[57] A. Denner and S. Pozzorini, *One loop leading logarithms in electroweak radiative corrections. 1. Results*, *Eur. Phys. J.* **C18** (2001) 461–480, [hep-ph/0010201].

[58] A. Denner and T. Hahn, *Radiative corrections to $W^+W^- \to W^+W^-$ in the electroweak standard model*, *Nucl. Phys.* **B525** (1998) 27–50, [hep-ph/9711302].

[59] **HL-LHC and HE-LHC Working Group** Collaboration, P. Azzi et al., *Standard Model Physics at the HL-LHC and HE-LHC*, arXiv:1902.04070.